Tapering enhanced superradiance with a planar magnetic undulator

L. Feigin,[1,†] A. Gover,[2] R. Minnes,[1] and A. Nause[1,*]
[1]*Ariel University, Department of Physics, Ariel 4076414*
[2]*Tel Aviv University, Center of Light-Matter Interaction, School of Electrical Engineering—Physical Electronics, Tel Aviv 69978, Israel*

(Received 13 May 2025; accepted 26 September 2025; published 19 November 2025)

Tapering enhanced superradiance (TES) is a novel radiation scheme that significantly improves the energy conversion efficiency in free-electron lasers. The undulator tapering design and optimization are crucial to the success of this efficiency boost and are fairly complicated tasks. Here, we demonstrate how to optimize the linear tapering rate using analytical magnetic field maps derived from pure permanent magnet (PPM) equations. A TES undulator (waveguided tapered undulator) is designed to operate at 0.5 THz at the zero-slippage regime, ensuring phase synchronicity and group velocity match between the electron beam and the radiation field. The superradiance condition is fulfilled by compressing the electron bunch to emit coherently. The results reveal a significant enhancement in energy conversion efficiency for both ideal and realistic beams. The real beam simulations use the ORGAD FEL parameters from the Schlesinger Accelerator Center at Ariel University. This work shows the potential of the TES method to achieve higher radiation energies through careful undulator design and optimized tapering and provides a complete model for this purpose.

DOI: 10.1103/ygzx-6my6

I. INTRODUCTION

ORGAD is a THz FEL located at Ariel University, which is designed to emit superradiantly with a dominant frequency of 3 THz [1–4]. Superradiance increases the radiation energy from an FEL by coherently summing the electrons' contribution, resulting in radiation power proportional to Q_b^2, while typical undulator radiation is proportional to Q_b [5]. As demonstrated by Musumeci *et al.* [6], the energy conversion efficiency of a superradiant FEL can be further improved by slowing down the interacting radiation field using a waveguide structure and attaining the zero-slippage condition, which ensures phase synchronization and group velocity match between the beam and the field. This new radiation scheme is named tapering enhanced superradiance (TES) [7]. In a TES radiation scheme, one can either taper the magnetic field amplitude or the undulator period. In our case, we model amplitude tapering, in which the distance of magnets from the beam axis is varied. This is a more practical method due to the magnets' similarity. Typically, a TES scheme requires initial seeding. However, unlike tapering enhanced stimulated superradiant amplification (TESSA) [8,9], the TES method does not rely on an external source, but rather a self-seeding alternative, making experimental synchronization much more simple [10,11]. A recently proposed tapering-enhanced high-efficiency THz waveguide oscillator aims to improve energy conversion efficiency in free-electron lasers (FELs). This oscillator has achieved energy conversion efficiencies of up to 16% in the high-efficiency regime for a frequency of 0.2 THz and 2.1% for a frequency of 1.5 THz [12]. However, similar to the TESSA approach, this method requires precise synchronization between the oscillating THz radiation field and the injected electron beams. In contrast, the TES radiation scheme is structurally and operationally simpler than the THz waveguide oscillator. The TES radiation scheme consists of two undulator sections: a uniform section and a tapered section. The uniform section generates the electric field radiation up to saturation, while the tapering section significantly increases the radiation field energy extraction by trapping the electron beam bunch in a slowing-down trap, and extending the radiation energy extraction. The TES emission process requires operating in the zero-slippage condition in order to avoid slippage of the bunch out of the trap. The zero-slippage condition refers to a state where the phase synchronicity and the longitudinal group velocity of the electron beam align with those of the radiation field along the undulator. Achieving this condition requires the use of a waveguide structure to reduce the group velocity of the radiation field [13]. Based on the dispersion equations for both the electron beam and the radiation field within a

*Contact author: arieln@ariel.ac.il
†Contact author: leonf@ariel.ac.il

Published by the American Physical Society under the terms of the Creative Commons Attribution 4.0 International license. Further distribution of this work must maintain attribution to the author(s) and the published article's title, journal citation, and DOI.

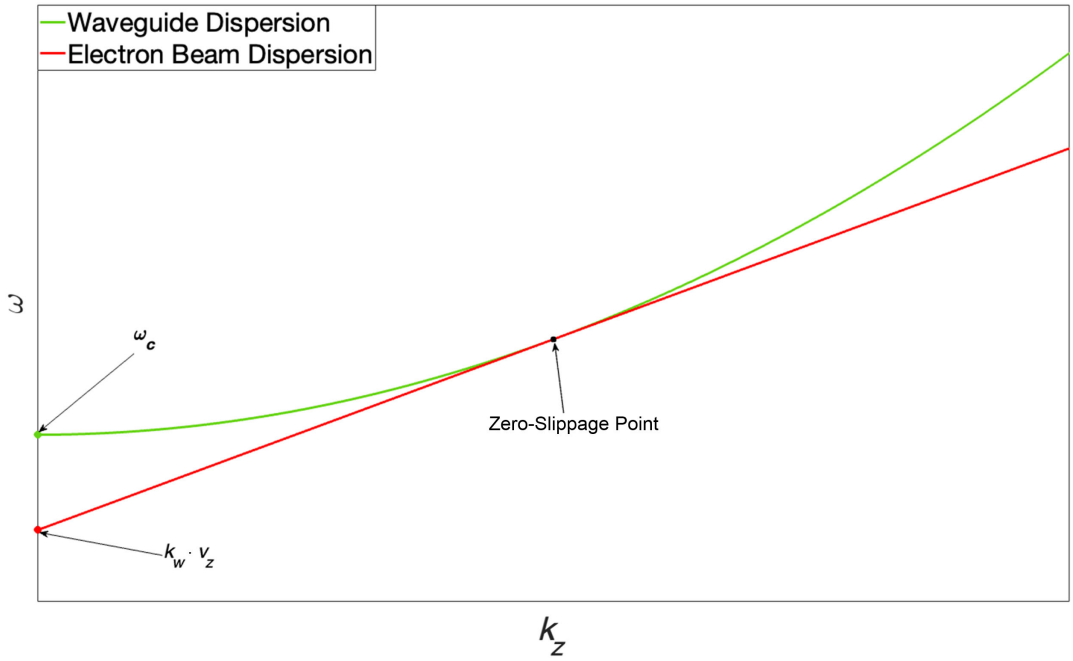


FIG. 1. Scheme of the dispersion curves of the radiation field in a waveguide structure and the electron beam dispersion curve. The zero-slippage condition is fulfilled when the e-beam dispersion curve is tangent to the radiation field dispersion curve.

waveguide, we can establish a direct relationship between the radiation frequency at zero slippage, the beam energy, and the dimensions of the waveguide [10]:

$$\omega_{r,zs} = \gamma_z \omega_c, \tag{1}$$

where $\omega_{r,zs}$ is the zero-slippage frequency of the radiation field, $\gamma_z = \sqrt{\frac{\gamma^2}{1+(\frac{K^2}{2})}}$ is the average beam energy, and ω_c is the waveguide's cut-off frequency, which depends on its dimensions. Illustration of the zero-slippage frequency is presented in Fig. 1.

The undulator field was modeled using bar magnet fields at different locations along its space, creating a complete field map that can be optimized by varying the magnets' location in space. Here, we present a design of a TES-FEL operating at 0.5 THz, based on a planar undulator. To achieve this, we relied on a model of a pure permanent magnet (PPM) waveguided undulator [14], where we adjusted the vertical position of each magnet to achieve the magnetic field amplitude tapering. Hybrid undulators, which combine PPMs and ferromagnetic materials, are commonly used to achieve high and stable magnetic fields [15–17]. However, the PPM magnet systems are simpler and have the advantage of using analytical equations to fully map the undulator magnetic field. In this paper, the TES scheme using the PPM undulator model and the tapering rate optimization methods are presented and explained for both ideal and nonideal electron beams. Note that nonideal beams that are strongly compressed in the longitudinal axis suffer from space-charge effects, causing a significant transverse divergence, and therefore, side-focusing magnets are incorporated in the final undulator design [18].

II. DESIGN AND CONSIDERATIONS OF A TAPERED PLANAR UNDULATOR BASED ON PERMANENT MAGNETS

The tapered undulator is designed to operate according to the tapering enhanced superradiance (TES) scheme (see Fig. 2). The TES process is composed of two stages. In the first stage, a short bunch electron beam emits Superradiant radiation in a waveguide FEL configuration. In the second stage, the electron bunch gets trapped in its own-generated radiation under the condition of waveguide mode group velocity synchronism with the beam velocity (zero-slippage condition) and tapering of the wiggler in a way that maintains phase velocity synchronism with the slowing down electrons. Superradiance is a coherent spontaneous synchrotron radiation obtained by an electron bunch precompressed into a state where the bunch duration (t_b) is shorter than the radiation period $(t_b << \frac{2\pi}{\omega})$ [5,10]. The figure of merit that determines the attainment of superradiance emission is the bunching factor, which is given for a Gaussian temporal distribution of the electron beam bunch by [5,19]:

$$M_b = e^{-\frac{\omega^2 \sigma_{tb}^2}{2}}, \tag{2}$$

where ω is the center radiation frequency, defined in the undulator system design, and σ_{tb} is the rms pulse duration

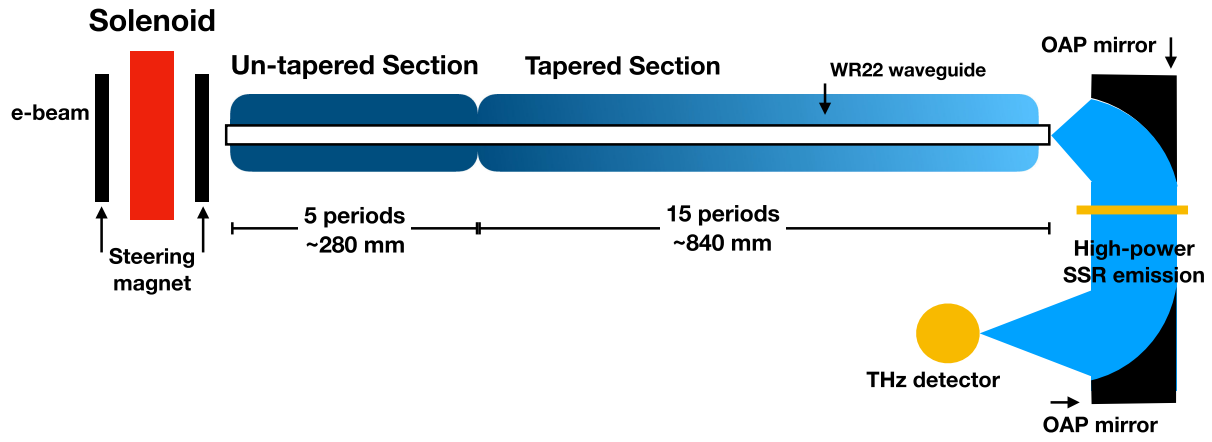


FIG. 2. Scheme of TES measurement system. Single waveguided undulator structure consists of 5 periods of uniform section + 15 periods of linear-tapering section, and a rectangular WR22 waveguide. The color gradient in the tapered section represents the variation of the undulator parameter K along this section (adapted from [10]).

of the electron beam. The superradiant radiation energy of the bunch is proportional to $|M_b|^2$. Evidently, the superradiant energy diminishes when $M_b < 1$, and for this reason, maintaining the short bunch condition $t_b << \frac{2\pi}{\omega}$ is a primary design requirement. We point out that the desirable tight longitudinal compression of the electron beam can cause its transverse divergence due to the space-charge effect. This is a critical factor in designing planar undulators, which typically have vertical weak focusing and no horizontal focusing. This issue becomes even more limiting when designing transport through a waveguide in which the cross section of the waveguide is small.

If the short bunch condition is satisfied, the radiative energy generated superradiantly in the first (uniform period) section of the two-part undulator grows quadratically as a function of the bunch charge and the undulator length ($\propto Q_b^2, N_w^2$).

After attaining substantial radiative energy in the uniform undulator section, the bunch can get trapped in the ponderomotive potential well at the entrance to the tapered undulator section, and with a moderate tapering rate, it stays trapped while the radiative energy grows on account of the dropping kinetic energy of the electron beam. In the case of magnetic amplitude tapering, the period of the tapered undulator is uniform ($k_w = \text{const}$), and therefore, the electron beam can keep synchronization with the phase of the ponderomotive potential [20]:

$$v_z = v_{ph} = \frac{\omega}{k_z + k_w}. \tag{3}$$

Though the axial velocity of the beam and the longitudinal component of its kinetic energy stay constant in the tapered section, energy extraction from the beam is facilitated on account of the transverse (wiggling) energy of the beam that drops down with the down tapering of the undulator field amplitude. The dynamics of the electrons within the ponderomotive trap are described in phase space by [5,20]:

$$\frac{d\gamma}{dz} = \frac{k_0 K(z) K_L}{2\gamma} \sin(\psi), \tag{4}$$

$$\frac{d\psi}{dz} = k_w + k_z - k_0 \left(1 + \frac{1 + \frac{K^2}{2}}{2\gamma^2}\right), \tag{5}$$

where ψ is the phase of the bunch relative to the ponderomotive potential.

The tapering of the undulator field is necessary in order to fulfill the zero-slippage condition, which synchronizes the phase and the longitudinal group velocity between the electron beam and the radiation field along the undulator, leading to an energy conversion efficiency enhancement after the electron bunch is trapped [21]. Since the group velocity in a waveguide is smaller than the speed of light, it is possible to obtain group velocity synchronism of a desirable waveguide mode by proper choice of the waveguide cross section parameters and cutoff frequency. In our case, we use a rectangular waveguide which matches the planar undulator's Cartesian symmetry. In our design, we use the scheme of magnetic field amplitude tapering. In this scheme, the periodicity of the undulator is uniform, and the phase and group synchronism are maintained with the constant axial velocity of the electron, while the transfer of energy from the beam to the wave comes on account of the transverse energy of the beam that reduces with the tapering down of the magnetic field amplitude and the consequent reduced wiggling amplitude. Amplitude tapering is a more practical approach than period tapering, and it simplifies the mechanical design of the undulator. In practice, this is achieved by adjusting the gap along the undulator. To ensure a smooth and continuous tapering effect, the gap is gradually varied after each successive magnet.

The TES is an unseeded radiation scheme that includes two undulator sections. The first section is a uniform undulator that generates superradiant radiation up to the point of saturation. This is immediately followed by a

tapered section that enhances the extraction of radiation from the beam. Importantly, these two radiating sections are not separate; they are constructed as a single undulator made up of both the uniform and tapered sections. Linear amplitude tapering of the wiggler is the simplest design option and is also the simplest model to be used in tapering design in an analytical model. If the radiation field (and consequently the depth of the ponderomotive potential trap) grow up along the tapered undulator, a more elaborate nonlinear tapering contours may provide better extraction efficiency, but in this work, we stay with a linear tapering model with a linear tapering rate set initially to keep synchronism of the ponderomotive potential trap assuming little increase of the trap depth along the interaction length. This analytically determined tapering rate is used as an initial trial in a numerical iterative process in which the tapering rate is modified with a target of maximizing the radiative extraction at the end of the undulator. This iterative optimization process, based on FEL-GPT simulations, takes into account the effect of radiative power amplification along the interaction length and longitudinal space-charge effect at high bunch charge.

The undulator amplitude tapering can be presented in terms of the undulator parameter (K) [22]

$$K(z) = \frac{eB_u(z)}{k_u m_e c}. \tag{6}$$

For a given trapping radiation field E_0, the tapering rate determines the phase ψ_r of the resonant electron in the electron beam distribution relative to the ponderomotive potential phase [10,23]:

$$\frac{dK}{dz} = -k_w K_L \sin(\psi_r), \tag{7}$$

where

$$K_L = \frac{eE_0}{mc^2 k_0} \tag{8}$$

is the normalized momentum of the electric field interacting with the electron beam, k_w is the undulator wave number, ψ_r is the resonance pondermotive phase, E_0 is the electric field amplitude at the transition point between the uniform and the tapered undulator sections, and k_0 is the free space wave number. Obviously, a higher tapering rate would provide higher energy extraction from the beam, but this is limited by the condition $\sin(\psi_r) < 1$. Moreover, in a finite energy and phase distribution of the electron bunch, the tapering should be small enough to keep most electrons within the trap without getting de-trapped. Therefore, beyond the necessary requirement of keeping the resonant electron trapped [Eq. (7)], full numerical simulation of the electron distribution dynamics in the trap is needed for optimization of the output radiation of a finite distribution bunch (see Sec. IV ahead).

Equation (7) is the starting point of the tapering rate iterative optimization process, which is carried out by evaluating first the radiation field amplitude (K_L) at the end of the uniform undulator section via GPT-FEL [24]. The resonance pondermotive phase is an arbitrarily chosen constant, which in our case is $\psi_r = (\pi/4)$ all along. The optimization consists of varying the tapering rate from each iteration to the next. While in the initial iteration step, the slope $(\frac{dK}{dz})_0$ was determined from Eq. (7) for the radiation parameter K_L that was evaluated at the end of the uniform undulator using GPT-FEL, in the next iteration steps GPT-FEL calculated the radiation output using a modified tapering rate:

$$\frac{dK}{dz} = f\left(\frac{dK}{dz}\right)_0, \tag{9}$$

where f is a constant, varied from step to step, indicating the radiative energy dependence on the tapering rate and resulting in the optimal rate for attaining maximal radiation output. The optimal tapering rate was evaluated for parameters of both ideal and realistic (ORGAD) electron beams, whereas, for the ideal beam case, we do not consider space-charge effects, while for the realistic beam, we do (see Sec. III).

A. Planar tapered undulator design

Pure permanent magnets (PPMs) have a significant advantage in attaining the magnetic field components in a 3D space. Most PPM-based planar undulators are designed using a bar magnet shape, which has analytical magnetic field formulas that can be used for 3D mapping of the undulator. The bar magnet equations are presented in Eqs. (10)–(12), where the magnetization of the bar is directed in the y axis, vertically to the beam propagation axis [25]:

$$H_x(x,y,z) = \frac{M_0}{4\pi}\sum_{k,l,m=1}^{2}(-1)^{k+l+m}\ln\left\{z+(-1)^m z_b + \sqrt{[x+(-1)^k x_b]^2+[y+(-1)^l y_b]^2+[z+(-1)^m z_b]^2}\right\}, \tag{10}$$

$$H_y(x,y,z) = \frac{M_0}{4\pi}\sum_{k,l,m=1}^{2}(-1)^{k+l+m}\frac{[y+(-1)^l y_b][x+(-1)^k x_b]}{|y+(-1)^l y_b||x+(-1)^k x_b|} \times \arctan\left\{\frac{|x+(-1)^k x_b|[z+(-1)^m z_b]}{|y+(-1^l)y_b|\cdot\sqrt{[x+(-1)^k x_b]^2+[y+(-1)^l y_b]^2+[z+(-1)^m z_b]^2}}\right\}, \tag{11}$$

$$H_z(x,y,z) = \frac{M_0}{4\pi}\sum_{k,l,m=1}^{2}(-1)^{k+l+m}\ln\left\{x+(-1)^k x_b+\sqrt{[x+(-1)^k x_b]^2+[y+(-1)^l y_b]^2+[z+(-1)^m z_b]^2}\right\}, \tag{12}$$

where H_x, H_y, and H_z are the magnetic field components, M_0 is the magnet's constant magnetization, x, y, and z are the spatial coordinates, and x_b, y_b, and z_b are the magnet's half lengths. The common Halbach array [14,26] also consists of magnets with magnetization oriented along the longitudinal axis (see Fig. 4). In the case of longitudinally magnetized magnets, we rotate the axes and obtain Eqs. (13)–(15):

$$H_x(x,y,z) = \frac{M_0}{4\pi}\sum_{k,l,m=1}^{2}(-1)^{k+l+m}\ln\left\{y+(-1)^m y_b+\sqrt{[x+(-1)^k x_b]^2+[y+(-1)^l y_b]^2+[z+(-1)^m z_b]^2}\right\}, \tag{13}$$

$$H_y(x,y,z) = \frac{M_0}{4\pi}\sum_{k,l,m=1}^{2}(-1)^{k+l+m}\ln\left\{x+(-1)^k x_b+\sqrt{[x+(-1)^k x_b]^2+[y+(-1)^l y_b]^2+[z+(-1)^m z_b]^2}\right\}, \tag{14}$$

$$H_z(x,y,z) = \frac{M_0}{4\pi}\sum_{k,l,m=1}^{2}(-1)^{k+l+m}\frac{[z+(-1)^l z_b][x+(-1)^k x_b]}{|z+(-1)^l z_b||x+(-1)^k x_b|} \times \arctan\left\{\frac{|x+(-1)^k x_b|[y+(-1)^m y_b]}{|z+(-1^l)z_b|\cdot\sqrt{[x+(-1)^k x_b]^2+[y+(-1)^l y_b]^2+[z+(-1)^m z_b]^2}}\right\}. \tag{15}$$

To validate the equations for the magnetic field of a permanent magnet, we created a prototype for a single Halbach period and measured the magnetic field in the undulator region. Figure 3 compares the on-axis magnetic field from our measurements with the results from CST simulations and the calculated values obtained from Eqs. (10) to (15).

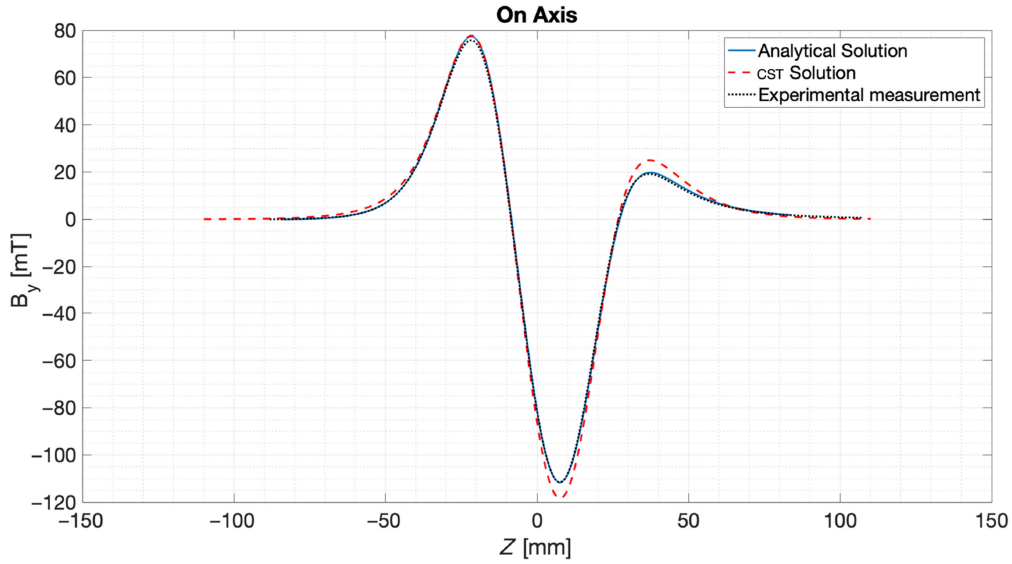


FIG. 3. Comparison of the on-axis magnetic field of a single Halbach period undulator prototype. The blue solid curve represents the analytical calculations, the red dashed curve is the CST simulation result, and the black dotted curve is the measurement results.

TABLE I. PPM properties.

Material	SmCo
Vertical magnet length (L_x)	40
Transverse magnet length (L_y) (mm)	10
Entrance magnets longitudinal length (L_z) (mm)	3 or 5
Undulator magnets longitudinal length (L_z) (mm)	10
Relative permeability (μ_r)	1.05
Remanent field (B_r) (T)	0.95
Magnetization ($M_0 = \frac{B_r}{\mu_0 \mu_r}$) ($\frac{\text{kA}}{\text{m}}$)	720

At the final stage, the 3D undulator magnetic field maps are incorporated into GPT in terms of magnetic field flux density (B). Therefore, Eqs. (10)–(15) are multiplied by the vacuum magnetic permeability constant to obtain valid results ($B = \mu_0 H$). The bar magnet properties used to construct the magnetic field map of a planar undulator are presented in Table I.

The undulator is designed according to the parameters provided in Table II and constructed using the bar magnet magnetic field components (10)–(15). The gap between the undulator jaws of the uniform section is 22.71 mm (see Fig. 4). The design of the entrance and exit magnets is based on Ref. [27] and optimized for our design. Optimization of the beam transport with GPT simulations required readjustments of the gap design of the entrance and exit magnets relative to the wiggler gap by an increment of 2 mm (Fig. 4) and 2.8 mm (Fig. 5), respectively. Additional adjustment of the gap of the exit magnets was required for different tapering rates.

The undulator is configured so that each magnet can be adjusted vertically, leading to a variation in the magnetic field along the axis. The benefit of a design where each magnet is mounted on a rail is that it allows for the correction of magnetic field variations due to manufacturing imperfections. The change in the magnetic field required for a linear tapering rate is evaluated by differentiating the undulator parameter K [10,22].

TABLE II. Undulator parameters.

Bunch energy (MeV)	6
Energy spread (rms) (%)	1
Bunch length (rms) (fs)	113–222
Beam charge (pC)	20–200
Undulator wavelength, λ_w (mm)	56
Undulator magnetic field, B_0 (K)	0.2195 T (1.1478)
Uniform undulator section gap (mm)	22.71
Spacing between adjacent magnets (mm)	4
Number of uniform undulator periods	5
Number of tapered undulator periods	15
Rectangular waveguide (WR22) (mm^2)	5.6896×2.8448
Mode cut-off frequency (GHz)	52.69
Peak THz (zero-slippage) frequency (THz)	0.52

$$\frac{dB}{dz} = \frac{mck_w}{e}\frac{dK}{dz}. \tag{16}$$

From Eq. (16), we construct a magnetic field array, which consists of five uniform undulator periods and another 15 tapered undulator periods, and determine the gaps between magnets accordingly. In the presented undulator, each undulator jaw consists of 83 magnets. Note that the amplitude tapering occurs up to the last magnet before the exit magnets array. To determine the relation between the gap size and the magnetic field on-axis B_0, we calculated the magnetic field on axis for different gap values using Eqs. (10)–(15). A logarithmic function that matches well the calculated dependence of gap vs B_0 within the practical field range is given by

$$\text{Gap} = a\ln(B_0) + b, \tag{17}$$

where $a = -0.0165$ m and $b = -0.0022$ m. The gap array was calculated using the magnetic field array according to Eq. (17), where the gap in the uniform section was set to 22.71 mm. Once the gap values of the tapered section were evaluated for a desired tapering rate, an additional small uniform increment of the gap of the entire tapered section was required in order to correct a simulated deflection of the beam at the transition between the uniform and tapered sections. This uniform gap increment of the tapered section had to be readjusted for different tapering rate values. After this gap-calibration process, we created a 3D magnetic field flux map using the final gap array, which was then integrated into GPT for particle-tracking simulations.

B. Lateral focusing side magnets

The previous design stages addressed an ideal electron beam and ignored space-charge effects in the electron beam. In order to consider a realistic case, we performed simulations for the parameters of our ORGAD accelerator beam (see beam parameters in Table II) and included full 3D space-charge effects in the GPT-FEL simulations. For beam charge $Q_b > 20$ pC, simulations showed severe effects of lateral divergence of the beam along the undulator. This divergence is attributed to the space-charge effect due to the strong longitudinal compression of the bunch and absence of lateral focusing in the configuration of a planar undulator. To overcome this problem, side magnets with vertical magnetization were added to create a quasiquadrupole focusing effect on the wiggling (horizontal) axis [18]. The side magnets do not alter the radiated energy or spectrum. They are not part of the radiating system, and they were mapped using the bar magnet magnetic field equations (10)–(12), according to the magnet parameters presented in Table III. The side magnets' center is positioned on the XZ plane with a fixed gap between their jaws on the horizontal (x) axis. A single-sided magnet jaw contains 36 bar magnets in an array,

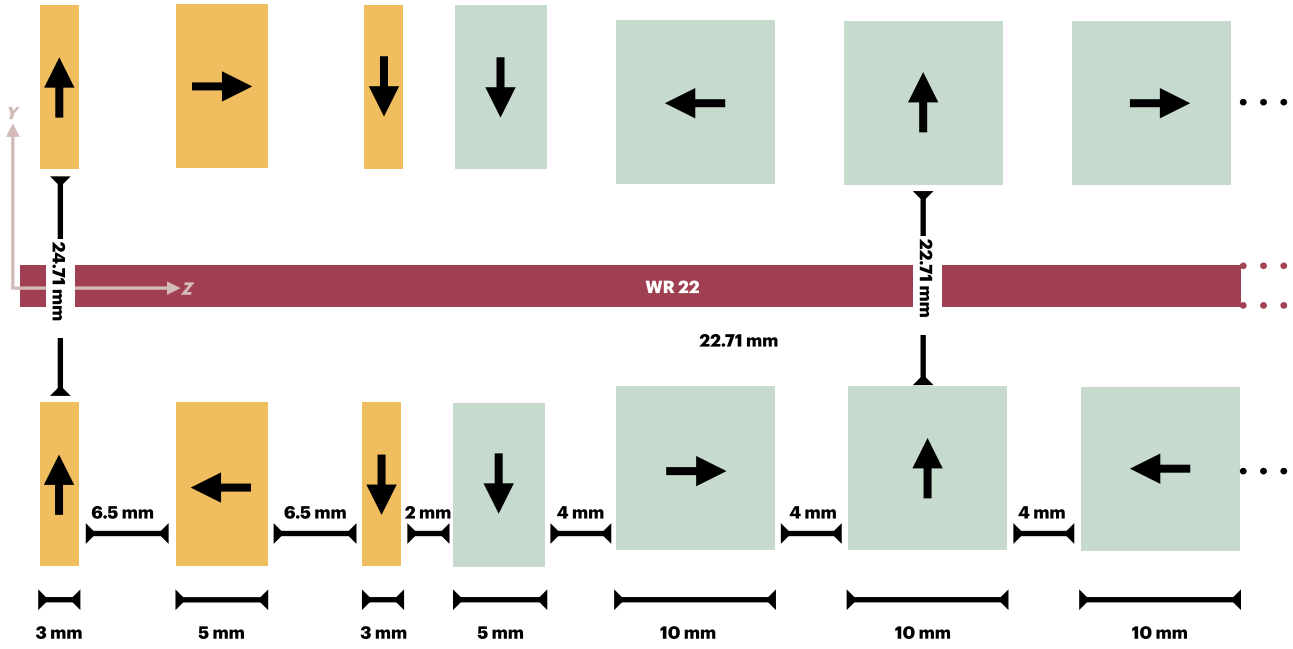


FIG. 4. Entrance magnets array (yellow blocks) followed by a uniform period undulator (green blocks).

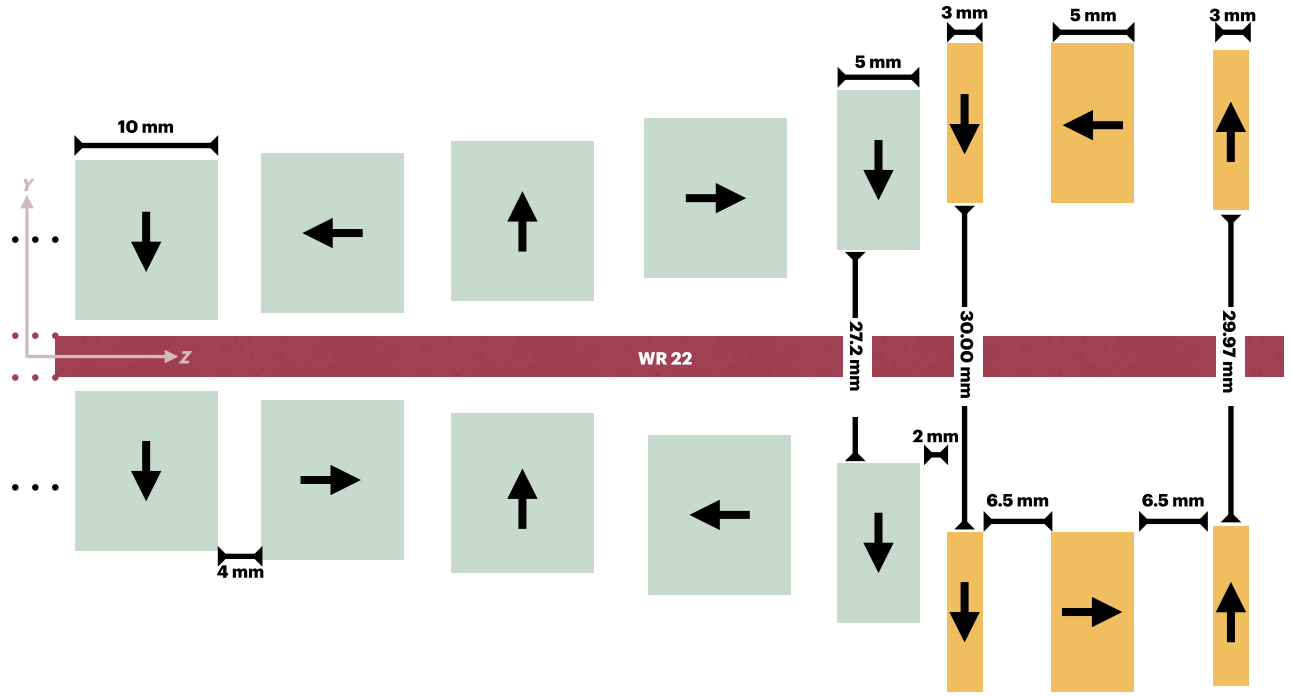


FIG. 5. Tapered undulator (green blocks) followed by an exit magnets array (yellow blocks).

where the magnetization of each successive magnet is opposite to the previous one. An illustration of the side magnets structure is presented in Fig. 6. The side magnets can be longitudinally adjusted to optimize position. Initially, each side magnet is co-centered with a vertically magnetized undulator magnet, such that the first side magnet is aligned to the first undulator magnet following the entrance magnets array. The side magnet structure is designed to longitudinally move up to 20 mm to each side with respect to its initial position. The adjustable position of the side magnets allows us to optimize their placement for the best focusing effect. Additionally, the design of the side magnets enables the replacement of magnets with different lengths (L_z), providing versatility and compatibility.

TABLE III. Side magnets parameters.

Material	SmCo
Vertical magnet length (L_x) (mm)	10
Transverse magnet length (L_y) (mm)	14
1st−10th side magnets length (mm)	14
11th−20th side magnets length (mm)	22
21st−36th side magnets length (mm)	28
Relative permeability (μ_r)	1.05
Remanent field (B_r) (T)	0.95
Magnetization $(M_0 = \frac{B_r}{\mu_0 \mu_r})$ $(\frac{\text{kA}}{\text{m}})$	720

For instance, we can substitute the first ten magnets, which have a length of $L_z = 14$ mm, with different magnets that have properties suited to a length of $L_z = 10$ mm. It is important to note that the transverse cross section (L_x and L_y) must remain consistent.

III. SIMULATION RESULTS

Here, we present particle-tracking simulation results of the fully optimized TES undulator. The tapering rate adjustment factor (f) was tuned in iterative simulation steps to obtain the highest energy conversion efficiency. This was carried out for both ideal and realistic electron beams. The energy conversion efficiency of a realistic beam is expected to differ significantly from that of an ideal beam. This divergence occurs because the ideal beam model does not account for space-charge effects. Additionally, without energy and phase distribution, the ideal beam represents only a perfectly longitudinally bunched beam ($M_b = 1$). Furthermore, the ideal beam has an atto-scale transverse cross section and does not experience longitudinal expansion while traveling through the undulator, unlike a realistic beam. The GPT-FEL simulations of a realistic beam include all the rf field maps of the ORGAD hybrid accelerator [1,2] starting from the cathode, the electron-optics magnetic field maps, and full 3D space-charge effects. All of these affect the electron beam properties, including the rms longitudinal and transverse bunch lengths. Because of the longitudinal bunch expansion due to the longitudinal space-charge effect, the bunching parameter $|M_b|$ of the beam is reduced in the first section of the undulator, with values from 78% to 96% for beam charge smaller than $Q_b < 200$ pC. The most damaging space-charge effect in the design of the TES structure with a realistic beam turned out to be the lateral beam expansion, which made it impossible to transport a high-charge beam through the small cross section of the waveguide without providing focusing means in the lateral dimension. This was facilitated by the side magnets structure described in Sec. II B. Once a proper choice of the beam cross section and the focusing parameters assures good transport through the 5.7×2.85 mm^2 cross section of the waveguide, the deteriorating effect at high beam charge is due to the longitudinal space-charge effect. The longitudinal expansion of the bunch diminishes the bunching factor in the first section of the undulator and enhances electrons' detrapping in the second section. In order to decrease the longitudinal expansion, the beam transverse cross section has an ellipsoidal shape, which reduces the transverse

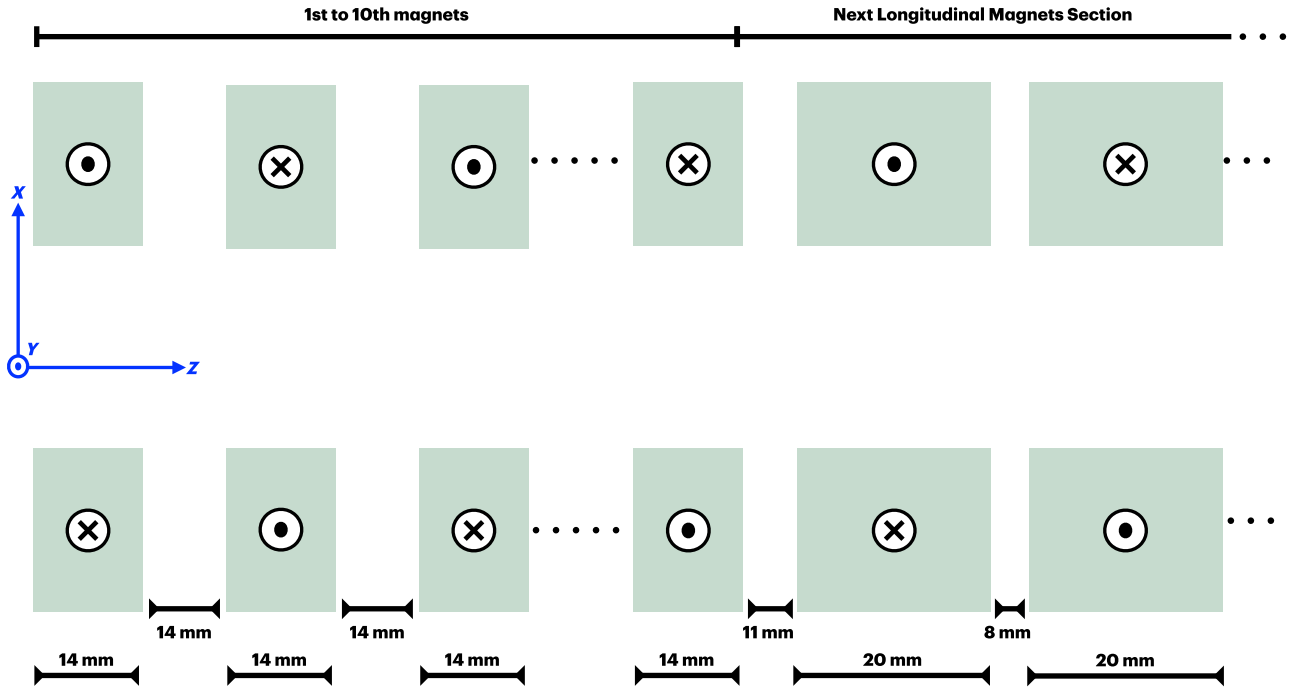
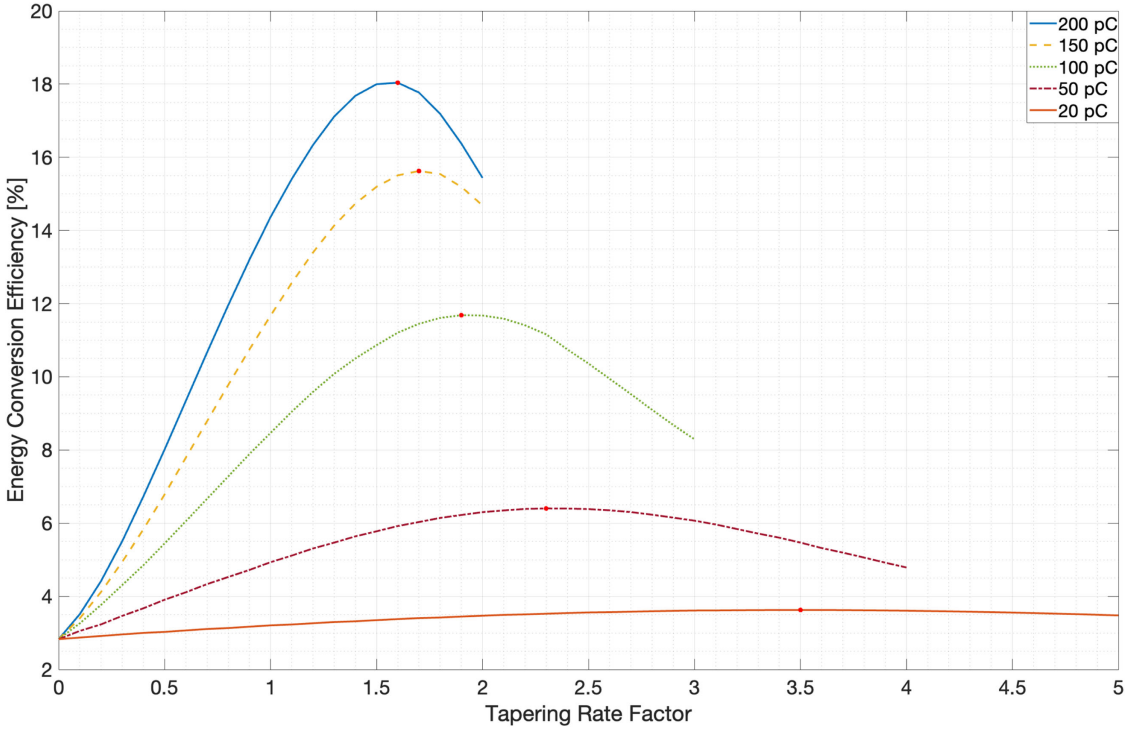
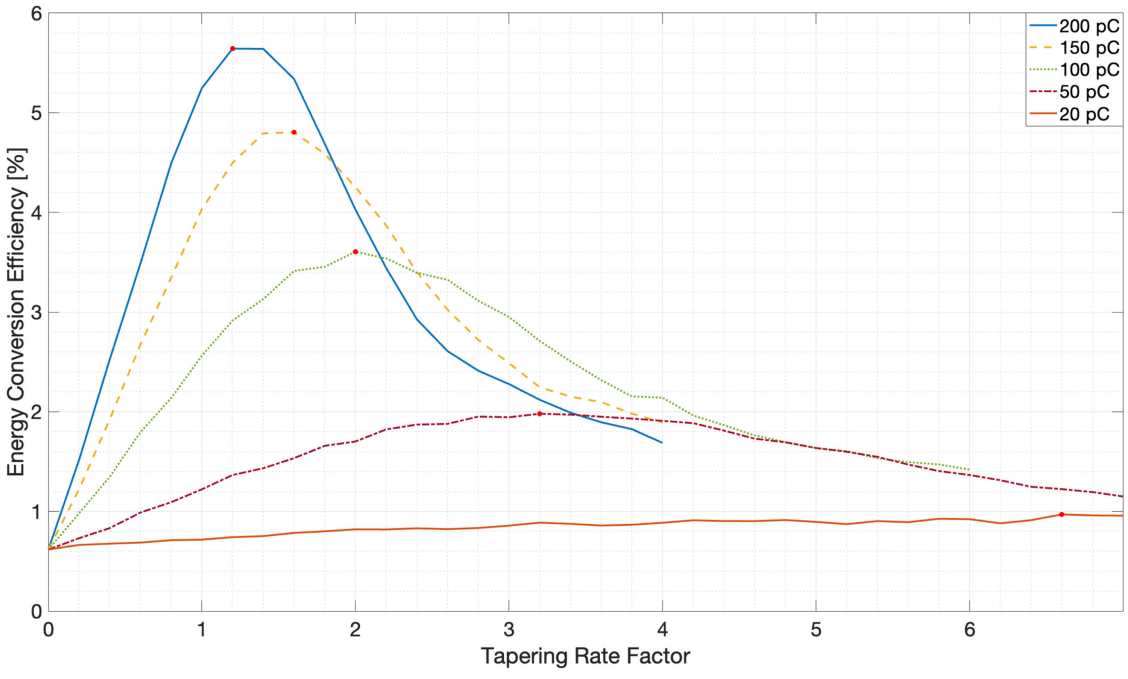


FIG. 6. Side magnets illustration.

space-charge effects. The electron beam transverse cross section is shaped using three quadrupoles that form a quadrupole triplet positioned before the undulator. In Fig. 7 we show the simulation results of the energy conversion efficiency vs the tapering rate factor for various beam charge values, comparing the two cases of ideal electron beam [Fig. 7(a)] and realistic electron beam [Fig. 7(b)]. As expected, the energy conversion efficiency values of the



(a)



(b)

FIG. 7. Energy conversion efficiency as a function of tapering rate factor for (a) an ideal beam and (b) a realistic beam. The red dots represent the optimal tapering rate factor values.

realistic parameters case are reduced relative to the ideal beam case.

In Table IV, we show the significant enhancement of energy extraction with a tapered wiggler in the TES scheme as compared to energy extraction in a uniform period wiggler of the same length (superradiance). The energy conversion increase presented is the ratio between the energy conversion efficiency at the optimal tapering rate factor ($\eta_{\max}$) and the energy conversion efficiency of the uniform undulator section (η_u).

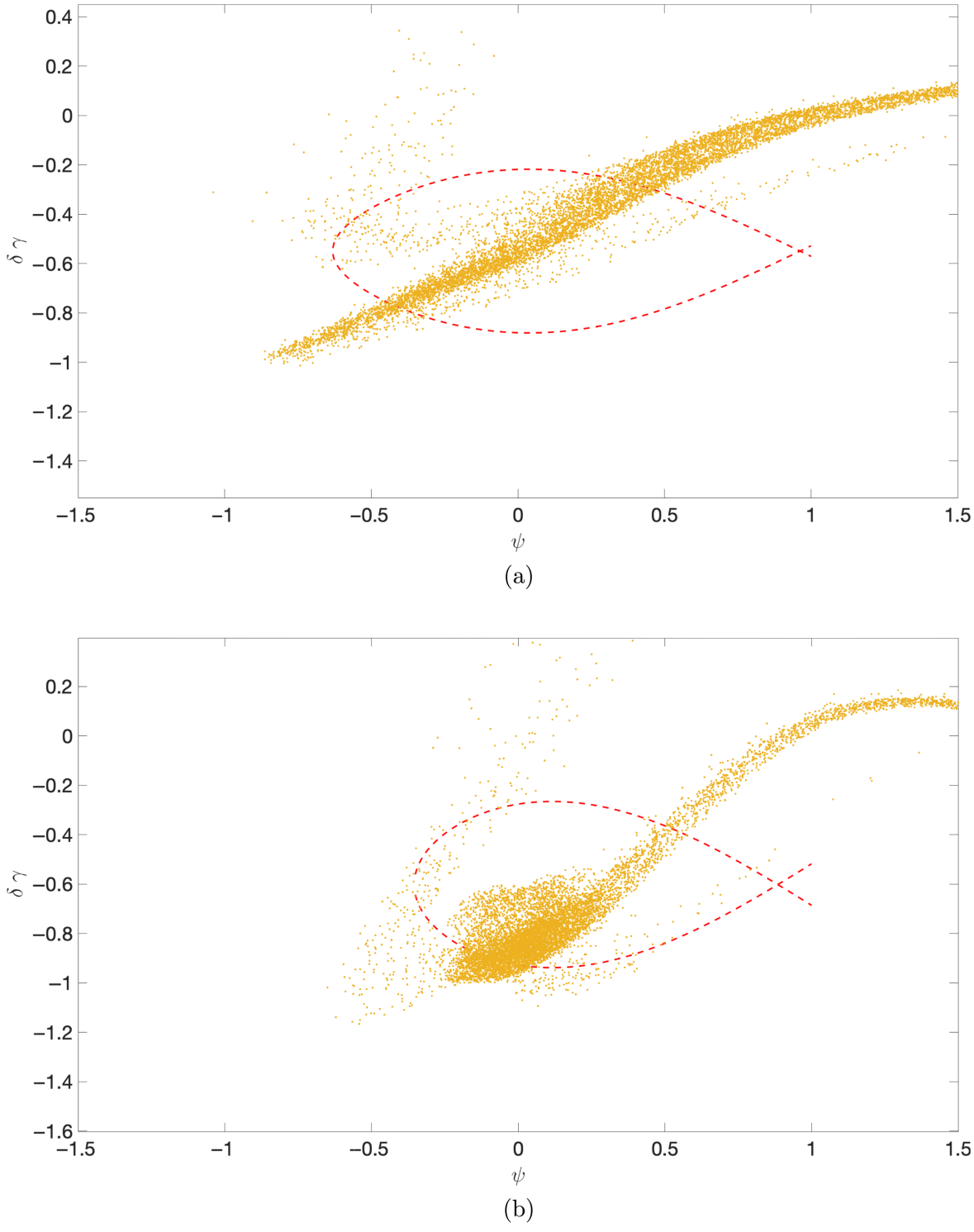


FIG. 8. Phase space of 100 pC electron beam bunch results for (a) unoptimized tapering rate, where the tapering rate factor is $f = 3$, and (b) optimized tapering rate, where the tapering rate factor is $f = 2$.

TABLE IV. Energy conversion efficiency enhancement in the TES scheme relative to a uniform period wiggler superradiance scheme for the case of a realistic electron beam.

Beam charge (pC)	Optimized tapering rate, $\frac{dK}{dz}$ (m^{-1})	Radiative energy (μJ)	Extraction efficiency (%)	Conversion efficiency increase ($\frac{\eta_{max}}{\eta_u}$) (%)
20	−0.1885	1.50	0.97	157
50	−0.1908	4.67	1.98	320
100	−0.1539	17.17	3.60	583
150	−0.1269	35.85	4.80	777
200	−0.1082	56.21	5.65	913

Figure 8 illustrates the phase-space dynamics of a finite, realistic beam distribution. It compares the phase-space distribution at the end of the tapered undulator in two cases: (a) unoptimized tapering, where the tapering rate is equal to 3, and (b) optimized tapering, where the tapering rate is equal to 2, as shown in Fig. 7(b).

IV. CONCLUSIONS

A pure permanent magnet (PPM) based waveguided tapered planar undulator was designed using PPM analytical equations and constructed 3D magnetic field maps. The waveguided tapered undulator is designed to operate in the zero-slippage regime in order to fulfill the synchronicity condition and group velocity match between the electron beam and radiation field. Moreover, we fulfill the superradiance condition, where the electron bunch duration is shorter than the radiation period. By fulfilling these conditions and by performing magnetic field amplitude tapering, we obtain tapering enhanced superradiance (TES) without any seed injection. For the case of a realistic (finite distribution) beam, a side magnet structure was incorporated in the beam transport design in order to focus the beam in the lateral dimension of the planar undulator and mitigate the lateral expansion of the beam due to the transverse space-charge effect. The linear tapering rate was optimized by GPT-FEL simulations to obtain the highest energy conversion efficiency. The results for both ideal and realistic beams show that up to $Q_b = 200$ pC, the energy conversion efficiency increases with beam charge due to the quadratic dependence of superradiance in the uniform period section and the tapering scheme in the tapered section. The results show that the tapering enhanced superradiance radiation scheme can lead to higher energy conversion efficiencies, yielding significantly higher radiation energies of up to hundreds of percent.

ACKNOWLEDGMENTS

This work was supported by the Israel Science Foundation Grant No. 1705/22.

DATA AVAILABILITY

The data are not publicly available. The data are available from the authors (Leon Feigin and Ariel Nause) upon reasonable request.

[1] A. Nause, A. Friedman, A. Weinberg, D. Borodin, L. Feigin, A. Fukasawa, J. Rosenzweig, R. Roussel, and B. Spataro, 6 MeV novel hybrid (standing wave—traveling wave) photo-cathode electron gun for a THz superradiant FEL, Nucl. Instrum. Methods Phys. Res., Sect. A **1010**, 165547 (2021).

[2] A. Nause, A. Friedman, A. Fukasawa, J. Rosenzweig, R. Roussel, and B. Spataro, First operation of a hybrid e-gun at the Schlesinger Center for Compact Accelerators in Ariel University, in *Proceedings of the 10th International Particle Accelerator Conference, Melbourne* (JACoW, Geneva, Switzerland, 2019), 10.18429/JACoW-IPAC2019-TUXXPLM3.

[3] L. Feigin, A. Weinberg, and A. Nause, Algorithm verification of single-shot relativistic emittance proposed measuring method, Electronics **11**, 2092 (2022).

[4] L. Feigin and A. Nause, Single-shot emittance measurement and optimization of a hybrid photo-cathode gun beam, Nucl. Instrum. Methods Phys. Res., Sect. A **1055**, 168539 (2023).

[5] A. Gover, Superradiant and stimulated-superradiant emission in prebunched electron-beam radiators. I. Formulation, Phys. Rev. ST Accel. Beams **8**, 030701 (2005).

[6] P. Musumeci, A. Fisher, A. Gover, E. Nanni, E. Snively, and B. van der Geer, A waveguide-based high efficiency Super-radiant FEL operating in the THz regime, in *Proceedings of the 39th International Free Electron Laser Conference, Hamburg, Germany* (JACoW, Geneva, Switzerland, 2019), TUP036, 10.18429/JACoW-FEL2019-TUP036.

[7] A. Gover and P. Sprangle, A unified theory of magnetic bremsstrahlung, electrostatic bremsstrahlung, Compton-Raman scattering, and Cerenkov-Smith-Purcell free-electron lasers, IEEE J. Quantum Electron. **17**, 1196 (1981).

[8] J. Duris, P. Musumeci, N. Sudar, A. Murokh, and A. Gover, Tapering enhanced stimulated superradiant oscillator, Phys. Rev. Accel. Beams **21**, 080705 (2018).

[9] J. Duris, A. Murokh, and P. Musumeci, Tapering enhanced stimulated superradiant amplification, New J. Phys. **17**, 063036 (2015).

[10] L. Feigin, A. Gover, A. Friedman, A. Weinberg, D. Azar, and A. Nause, High-power terahertz free electron laser via tapering-enhanced superradiance, Electronics **13**, 1171 (2024).

[11] A. Fisher, M. Lenz, A. Ody, Y. Yang, C. Pennington, J. Maxson, T. Hodgetts, R. Agustsson, A. Murokh, and P. Musumeci, Towards higher frequencies in a compact prebunched waveguide THz-FEL, Nat. Commun. **15**, 7582 (2024).

[12] Y. N. Yang, A. Fisher, P. Musumeci, R. K. Li, M. Kravchenko, R. Agustsson, Y. Chen, and A. Murokh,

Tapering-enhanced high-efficiency THz waveguide oscillator, Phys. Rev. Accel. Beams **27**, 100701 (2024).

[13] E. Curry, S. Fabbri, P. Musumeci, and A. Gover, THz-driven zero-slippage IFEL scheme for phase space manipulation, New J. Phys. **18**, 113045 (2016).

[14] K. Halbach, Design of permanent multipole magnets with oriented rare earth cobalt material, Nucl. Instrum. Methods **169**, 1 (1980).

[15] K. Robinson, D. Quimby, J. Slater, T. Churchill, A. Pindroh, and A. Valla, Hybrid undulator design considerations, Nucl. Instrum. Methods Phys. Res., Sect. A **250**, 100 (1986).

[16] V. Papadichev and G. Rybalchenko, End field formation in planar hybrid undulators to ensure gap independence of the first and second field integrals, Nucl. Instrum. Methods Phys. Res., Sect. A **532**, 644 (2004).

[17] I. B. Vasserman, S. Sasaki, R. J. Dejus, O. A. Makarov, E. R. Moog, E. M. Trakhtenberg, and N. A. Vinokurov, Magnetic measurements and tuning of the LCLS prototype undulator, Nucl. Instrum. Methods Phys. Res., Sect. A **507**, 191 (2003), Proceedings of the 24th International Free Electron Laser Conference and the 9th Users Workshop.

[18] A. A. Varfolomeev, V. V. Gubankov, A. H. Hairetdinov, S. N. Ivanchenkov, A. S. Khlebnikov, N. S. Osmanov, and S. V. Tolmachev, Mock-up of the focusing undulator for the SLAC x-ray FEL project, Nucl. Instrum. Methods Phys. Res., Sect. A **358**, 70 (1995).

[19] A. Gover, R. Ianconescu, A. Friedman, C. Emma, and P. Musumeci, Coherent emission from a bunched electron beam: Superradiance and stimulated-superradiance in a uniform and tapered wiggler FEL, Nucl. Instrum. Methods Phys. Res., Sect. A **865**, 25 (2017).

[20] A. Gover, R. Ianconescu, A. Friedman, C. Emma, N. Sudar, P. Musumeci, and C. Pellegrini, Superradiant and stimulated-superradiant emission of bunched electron beams, Rev. Mod. Phys. **91**, 035003 (2019).

[21] E. Snively, *Electron-THz Wave Interactions in a Guided Inverse Free Electron Laser* (University of California, Los Angeles, 2018), https://books.google.co.il/books?id=hsEWzgEACAAJ.

[22] P. Schmüser, M. Dohlus, J. Rossbach, and C. Behrens, *Free-Electron Lasers in the Ultraviolet and X-Ray Regime* (Springer International Publishing, 2014), 10.1007/978-3-319-04081-3.

[23] A. Fisher, M. Lenz, A. Ody, Y. Yang, C. Pennington, J. Maxson, T. Hodgetts, R. Agustsson, A. Murokh, and P. Musumeci, Towards higher frequencies in a compact prebunched waveguide THz-FEL, Nat. Commun. **15**, 7582 (2024).

[24] A. Fisher, P. Musumeci, and S. B. Van der Geer, Self-consistent numerical approach to track particles in free electron laser interaction with electromagnetic field modes, Phys. Rev. Accel. Beams **23**, 110702 (2020).

[25] R. Engel-Herbert and T. Hesjedal, Calculation of the magnetic stray field of a uniaxial magnetic domain, J. Appl. Phys. **97**, 074504 (2005).

[26] K. Halbach, Application of permanent magnets in accelerators and electron storage rings (invited), J. Appl. Phys. **57**, 3605 (1985).

[27] R. D. Schlueter, S. Marks, and S. Prestemon, Elliptically polarizing undulator end designs, IEEE Trans. Appl. Supercond. **16**, 1582 (2006).